Direct numerical simulation of hydrogen-enriched lean premixed methane–air flames

Evatt R. Hawkes [*], Jacqueline H. Chen

Reacting Flow Research Department, Combustion Research Facility, Sandia National Laboratories, P.O. Box 969 MS 9051, Livermore, CA 94551-0969, USA

Abstract

The effect of hydrogen blending on lean premixed methane–air flames is studied with the direct numerical simulation (DNS) approach coupled with a reduced chemical mechanism. Two flames are compared with respect to stability and pollutant formation characteristics—one a pure methane flame close to the lean limit, and one enriched with hydrogen. The stability of the flame is quantified in terms of the turbulent flame speed. A higher speed is observed for the hydrogen-enriched flame consistent with extended blow-off stability limits found in measurements. The greater flame speed is the result of a combination of higher laminar flame speed, enhanced area generation, and greater burning rate per unit area. Preferential diffusion of hydrogen coupled with shorter flame time scales accounts for the enhanced flame surface area. In particular, the enriched flame is less diffusive-thermally stable and more resistant to quenching than the pure methane flame, resulting in a greater flame area generation. The burning rate per unit area correlates strongly with curvature as a result of preferential diffusion effects focusing fuel at positive cusps. Lower CO emissions per unit fuel consumption are observed for the enriched flame, consistent with experimental data. CO production is greatest in regions which undergo significant downstream interaction. In these regions, the enriched flame exhibits faster oxidation rates as a result of higher levels of OH concentration. NO emissions are increased for the enriched flame as a result of locally higher temperature and radical concentrations found in cusp regions.
Published by Elsevier Inc. on behalf of The Combustion Institute.

Keywords: Lean premixed combustion; Hydrogen; Methane; Direct numerical simulation

1. Introduction

Lean premixed combustion (LPC) of natural gas in gas turbines has the potential to produce power with low emissions of oxides of nitrogen (NO_x), owing largely to the lower combustion-zone temperatures. Lower combustion-zone temperatures result in reduced NO_x levels from the Zeldovich thermal mech-

anism (e.g., [1]). However, the reduction in flame temperature results in weaker flames that are closer to the lean flammability limit and more sensitive to turbulent flow and composition variations. Ultralean flames are plagued by susceptibility to local extinction and quenching, leading to problems such as flame blowout, poor combustion efficiency, acoustic combustion instabilities, and elevated levels of carbon monoxide (CO) and unburned hydrocarbons (UHC).

Premixed combustion of hydrogen gas (H_2) in air exhibits a faster laminar flame speed and a lower lean flammability limit than methane (the primary component of natural gas). In addition, H_2 is highly diffu-

* Corresponding author. Fax: (925) 294 2595.
E-mail address: erhawke@ca.sandia.gov
(E.R. Hawkes).

sive, which can augment the resistance of the flame to the influence of turbulent stretch. These observations lead to the possibility that the addition of small amounts of H_2 to the fuel could result in enhanced flame stability. Enhanced stability might then result in reduced CO and UHC emissions. Addition of H_2 might be expected to have a negative impact on NO emissions due to higher flame temperatures; however this may be offset by the ability to burn an overall leaner mixture.

There have been several practical investigations of H_2 enrichment in various combustion applications. Use of H_2-enriched fuels has been found to extend the lean operating or stability limit and reduce emissions of NO_x, UHC, and CO in spark-ignited engines [2], aircraft gas turbines [3], and gas turbines for power generation [4–6].

There have been several studies of a more fundamental nature that have shed light on issues associated with flame stability [7–13]. In summary, these works have shown that lean H_2-enriched flames exhibit a somewhat higher laminar flame speed, an extended lean flammability limit, and a greatly enhanced resistance to strain. Unsteady one-dimensional simulations [14,15] have emphasized the importance of the flame timescale with regard to the transient response. Recent experiments in a swirl-stabilized burner [16, 17] at atmospheric pressure have been conducted to quantify the effects of H_2 addition under fuel-lean conditions. Flame blowout and stability characteristics were investigated, demonstrating a significant extension of the lean stability limit.

Some studies have also investigated the influence of H_2 blending on CO emissions. For strained flames, [12] found lower CO leakage from the reaction zone and attributed this to the increased radical pool. A systematic numerical study of the effects of H_2 blending on CO emissions has been conducted [18]. It was found that CO levels are quite insensitive to H_2 enrichment for freely propagating flames. A reaction-path analysis indicated little change in the overall CO reaction paths for up to 20% H_2 blending by volume, with the reaction $OH + CO \Leftrightarrow CO_2 + H$ almost entirely responsible for CO consumption. The rate of this reaction increases with H_2 blending, but so does conversion of the fuel to CO, resulting in the observed insensitivity. It was remarked that the experimentally observed behavior of CO near the blow-off limit was not captured by these steady simulations.

NO_x emissions have also been studied for steady strained flames. For leaner mixtures [19] found a slight increase in the maximum NO_x with H_2 blending in both experiments and calculations. However, for mixtures having the same flame speed (an indicator of flame stability), reduced NO_x emissions were reported. The decrease was associated with a re-

duced contribution of the prompt NO_x mechanism. NO_x formation paths were also studied in [18], and it was found that the reaction path in a freely propagating flame was somewhat invariant to the level of H_2 blending, but did depend on equivalence ratio. The swirl-stabilized burner experiments of [16,17] report higher NO_x levels early in the flame, but nearly equal levels further downstream.

To date, computational studies of H_2-enriched flames have been performed in steady and unsteady one-dimensional flame configurations. These studies have provided valuable insight into the effects that might promote a more stable flame: higher laminar flame speed, lower lean flammability limit, and greater resistance to strain and extinction. However, it is unclear how these effects will translate into a more stable flame in an unsteady turbulent environment. For example, it has been shown in theory [20] and in simulations (e.g., [21]) that Lewis number effects disappear in the high-frequency limit for a one-dimensional strained flame. Also, direct numerical simulations (DNS) of methane–air flames [22] have shown a decrease of the Markstein number for flame strain with increasing turbulence intensity. Thus it is possible that the influence of the high diffusivity of H_2 will be diminished in a turbulent environment.

Flames under unsteady strain can be strained beyond the steady extinction limit at sufficiently high frequencies relative to the flame time scale [23]. Thus it might be expected that since H_2-enriched flames have a shorter time scale they may respond more quickly to the unsteadiness, resulting in narrowing of the gap in extinction strain rate for unsteady strain conditions.

Also, it is not clear to what extent a higher laminar flame speed translates into a higher turbulent flame speed. For example, DNS [24] has shown that the role of laminar propagation in a turbulent flame is on average to reduce flame area, possibly reducing the difference between the turbulent flame speeds of enriched and pure methane flames. Moreover, flame area generation and destruction mechanisms are fundamentally multidimensional and unsteady.

Flames subjected to sufficiently high turbulence intensity fall into the so-called thin reaction zones regime [25], where small turbulent eddies can penetrate the preheat zone but not the inner reaction layer. In this regime Peters [25] has shown that turbulent effects on the flame structure are dominated by the flame curvature—an influence that cannot be studied in the planar counterflow configuration.

Emissions of CO have been shown to be insensitive to H_2 blending for freely propagating flames [18]; however, it is known that blending does reduce CO emissions in practice [17]. CO emissions in lean combustion are thought to arise in large part from

extinction, and this needs to be studied using an unsteady multidimensional simulation. Also, the mechanisms that lead to NO_x formation may be different in a turbulent environment owing to possible regions of locally high temperature and radical concentrations.

Thus there is a need for investigation of fundamental mechanisms that may contribute to the stability and emissions characteristics of H_2-enriched flames in an unsteady multidimensional environment. In this study a two-dimensional complex chemistry direct numerical simulation (DNS) of freely propagating flames interacting with an approximation to decaying homogeneous isotropic turbulence is chosen as the tool to investigate these mechanisms. Owing to computational expense, the technique of DNS is limited to a small range of length and time scales compared with those that occur in a practical burner. Therefore it is not possible to definitively understand all of the mechanisms that contribute to flame behavior. Mechanisms such as large-scale flow transients and mean shear, fluctuating mixture composition, recirculation, and heat losses that occur on the large scales are beyond the scope of DNS and may be more effectively studied with tools such as large eddy simulation (LES). However, using DNS it is possible to extract, under controlled conditions, high-quality information regarding small-scale flame behavior. This information is used here to help develop a fundamental understanding of the effects of H_2 enrichment in a turbulent environment. This understanding may be further employed to help interpret experimental results and provide modeling information for LES.

In this study a comparison is made between simulations of two lean premixed flames—one a pure methane flame close to the lean limit ($\phi = 0.52$), the other having the same equivalence ratio (based on the total mole fraction of fuel) but diluted with 29% H_2 on a molar basis. These mixtures were chosen to correspond to two cases considered in the swirl-stabilized burner experiments of Schefer et al. [17]. Here a numerical experiment is conducted—the two flames with different mixtures are subjected to an initially identical random two-dimensional flow field. The differences that are observed between the flames can then be attributed solely to the difference between the mixtures.

The main objective of this study is to compare the two flames with respect to flame characteristics that are important in assessing the utility of H_2-enriched fuels in lean premixed combustors. The primary purpose for the addition of H_2 is to enhance flame stability, and greater stability in terms of flame blow-off may be promoted by a higher turbulent flame speed. (Note that it is unclear whether this will help with problems of acoustic flame instability or flashback, except perhaps where the phenomena are coupled.)

Therefore three mechanisms that may be important to this end are studied. First, there is a contribution from a higher laminar flame speed that has previously been studied; second, there is a contribution from additional flame area generation due to thermal-diffusive mechanisms and resistance to extinction; and third, there is a local response of the flame structure to turbulent stretch. These mechanisms are studied here using both the global flame response and statistics taken from a methane isosurface representing the flame. The idea behind using LPC is ultimately to reduce pollutant emissions, so these are also considered. Mechanisms of CO and NO formation are studied in an unsteady turbulent environment (under fuel-lean conditions over 90% of the NO_x is NO [19]).

In addition, to our knowledge there have been no other studies with DNS of premixed combustion of multicomponent fuel mixtures with different diffusivities, nor of methane flames so close to the lean limit. This work presents an opportunity to begin to understand the interaction of these flames with unsteady turbulent stretch.

2. Formulation and numerical method

The two DNS simulations were initialized from a freely propagating planar flame solution, which is then strained and wrinkled by a random two-dimensional flow field imposed at the beginning of the simulation. The initial unsteady flow field is prescribed by a two-dimensional turbulent kinetic energy spectrum [26]. Initially the imposed fields are identical for both cases. The turbulence intensity in all cases was 1.5 m/s, which represents a level of approximately 10% of the mean flow speed in the experiments of [17].

The two-dimensional approximation is necessary to limit the computational expense since complex chemistry is considered. Two-dimensional turbulence differs from three-dimensional turbulence, namely by the absence of the vortex stretching mechanism; however, turbulent curvature statistics suggest that the most likely flame geometry is two-dimensional [27]. The fundamental interaction between the unsteady flow and the flame is expected to be captured in two dimensions, particularly in terms of the comparison of the two flames.

The turbulence and laminar flame parameters are summarized in Tables 1 and 2. In these tables, ϕ represents the equivalence ratio defined for the multicomponent fuel, defined as $\phi = [(X_{CH_4} + X_{H_2})/X_{O_2}]/[(X_{CH_4} + X_{H_2})/X_{O_2}]_{stoich.}$, where X is the species molar concentration. The symbol T_u represents the ambient fresh gas temperature, P_0 the ambient pressure, u' the root-mean-square ve-

Table 1
Initial turbulence parameters in DNS

Case	ϕ	T_u (K)	P_0 (kPa)	u' (m/s)	L_{11} (mm)	$Re_{L_{11}}$	L_x	L_y	$\delta_x = \delta_y$ (µm)
A, B	0.52	300	101	1.5	1.5	143	1.2	3.0	25

Table 2
Flame parameters in DNS

Case	$n_{H_2} = \dfrac{X_{H_2}}{X_{H_2} + X_{CH_4}}$	s_L (cm/s)	δ_{th} (mm)	u'/s_L (initial)	u'/s_L (final)	L_{11}/δ_{th} (initial)	L_{11}/δ_{th} (final)
A	0.0	5.27	1.77	28.5	22.6	0.85	1.33
B	0.29	7.58	1.31	19.8	16.5	1.14	1.57

locity fluctuation, L_{11} the turbulence integral scale based on two-point velocity correlations, and $Re_{L_{11}}$ the Reynolds number based on the L_{11} scale and unburned conditions. In Table 2, "initial" refers to conditions at the beginning of the simulation, "final" refers to conditions at two eddy turnover times, where the eddy turnover time is based on the initial L_{11} integral scale, and u'—results for this snapshot in time are used throughout the paper unless stated otherwise. The sizes of the domain in the initial flame normal and parallel directions are L_x and L_y respectively. The computational grid widths are given by δ_x and δ_y. The symbol s_L represents the unstrained laminar flame speed. The thermal thickness of the laminar flame is denoted by δ_{th}, where $\delta_{th} \equiv (T_{max} - T_u)/|\partial T/\partial x_i|_{max}$, and T_{max} refers to the maximum flame temperature. Note that using the Zeldovich thickness, $\delta_Z = D/s_L$, where D is the methane diffusivity, results in a smaller value: $\delta_Z \approx 0.3\delta_{th}$. The turbulence timescale is defined as L_{11}/u', and the thermal flame time is defined as $\tau_{th} = \delta_{th}/s_L$. In these simulations, the thermal thickness and integral scale are comparable, so large eddies can penetrate the preheat zone; however, the heat-release zone is substantially thinner than the integral scale and turbulent eddies do not penetrate this zone, placing the conditions within the thin reaction zones regime [25].

The DNS code solves the Navier–Stokes, species, and energy conservation equations for a compressible reacting gas mixture. The numerical scheme employs an eighth-order centered finite difference stencil for spatial differencing [28] and explicit fourth-order six-stage low-storage Runge–Kutta method for time advancement [29]. A modified version of the Navier–Stokes characteristic boundary condition treatment [30] is applied. Boundary conditions are periodic in the direction perpendicular to the initial propagation and nonreflecting in the other directions.

The present chemical mechanism consists of 19 chemical species and 15 reaction steps and is described in Section 3. The transported chemical species

Table 3
Species Lewis numbers

Species	Le	Species	Le
H_2	0.29	CO	1.09
H	0.18	CO_2	1.39
O	0.69	CH_2O	1.34
O_2	1.10	C_2H_2	1.31
OH	0.71	C_2H_4	1.34
H_2O	0.89	C_2H_6	1.47
HO_2	1.08	NO	1.09
H_2O_2	1.09	HCN	1.35
CH_3	0.99	N_2	1.04
CH_4	0.98		

are H_2, H, O, O_2, OH, H_2O, HO_2, H_2O_2, CH_3, CH_4, CO, CO_2, CH_2O, C_2H_2, C_2H_4, C_2H_6, NO, HCN, and N_2. The species mass diffusion is determined by prescribing the Lewis numbers of individual species [31]. Lewis numbers are determined from a best fit to the mixture-averaged transport coefficients recommended for the GRI3.0 mechanism [32] in the laminar flame and are given in Table 3. For the sake of efficiency, thermal diffusion has been neglected in these simulations. However, it is expected that its influence would be to enhance the conclusions presented in this paper, since it tends to promote diffusion of light molecules toward hot regions of the flame, increasing the H_2 focusing effect that is shown to be central to the conclusions of the paper.

Radiation is modeled with an optically thin assumption, taking CO_2, H_2O, CO, and CH_4 to be the only important radiating species. Plank mean absorption coefficients are obtained from the fit provided in [33].

To support the DNS calculations, steady laminar calculations are also conducted. Freely propagating flames are studied using PREMIX [34], modified to include the optically thin radiation model. Strained flames are studied using a modified version of OPPDIF [35]. These codes are interfaced with CHEMKIN [36] and TRANSPORT [37].

3. Chemical mechanism

The chemical mechanism is an augmented re-
duced mechanism (ARM) and has been provided by
C.J. Sung. It is based on the GRI mechanism 3.0
[32], but assumes that many of the species are in
steady state—that is, that the rates of production and
consumption are much greater in magnitude than the
net rate of change of the species concentration. The
mechanism employed here is very similar to those de-
scribed and validated in [38], in particular the 14-step
mechanism of that work. The main difference is that
in the present mechanism, the steady-state assump-
tion for the O radical has been relaxed. The reason
for this change is that, while a steady-state assump-
tion for O may be valid for pure methane combustion,
it has been shown to be inadequate in H_2 combus-
tion [39]. Also, there has been a recent a posteriori
justification of our choice in [40], which compared
the simulations of vortex ring nonpremixed CH_4/H_2
flames using reduced mechanisms against the GRI
mechanisms. They attributed discrepancies in ignition
delay times between the reduced and detailed mecha-
nisms to the steady-state assumption for the O radical
and recommended that this assumption be relaxed for
the application of reduced mechanisms to CH_4/H_2
flames.

There has been some experimental validation for
the use of GRI-based mechanisms for H_2-enriched
methane–air flames. GRI-3.0 was used by [9,12,19],
and very good agreement was obtained for laminar
flame speeds, NO_x levels, profiles of major species,
and extinction strain rates. GRI-2.11 and a reduced
mechanism [41] were used in [13]. They found close
agreement over a wide range of mixture conditions
for extinction strain rates using GRI-2.11, and slightly
poorer, but still good agreement using the reduced
mechanism. Note that the mechanism employed in the
present work represents an improvement over that in
[41], as outlined in [38].

Since experimental validation of the GRI mech-
anism for CH_4–H_2 flames has been performed else-
where, it suffices to show here that the reduced mech-
anism compares well with the full GRI mechanism.
To this end freely propagating flame calculations
are performed with the PREMIX code [34]. For the
mixtures considered, laminar flame speeds agreed to
within less than 1%, which is probably comparable
to numerical error. Temperature is shown in Fig. 1
and CO mass fraction in Fig. 2. The excellent agree-
ment is evident. NO mass fraction is shown in Fig. 3.
The reduced mechanism overpredicts NO somewhat
(relative to GRI-3.0), but does seem to capture the
qualitative effect of H_2 addition. Tests with the 17-
step mechanism of [38] showed some improvement
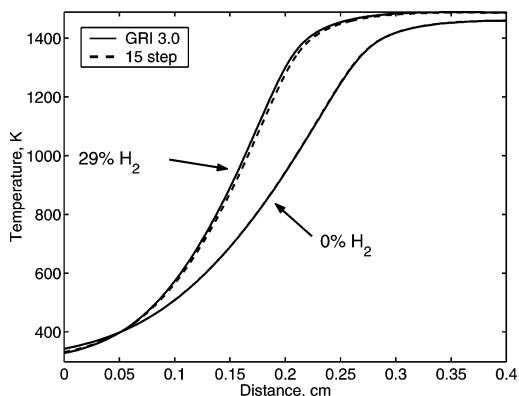in this overprediction, indicating that the cause of the

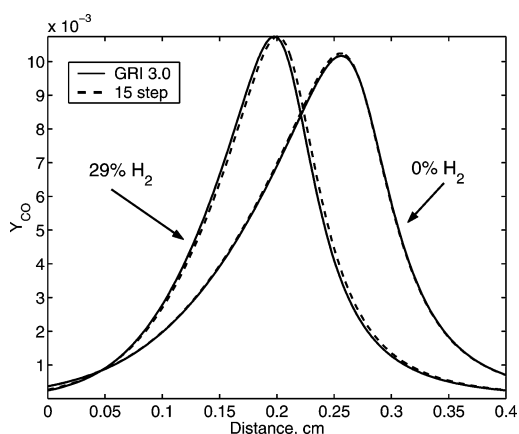Fig. 1. Temperature versus distance for GRI-3.0 and 15-step
mechanism.

Fig. 2. CO mass fraction versus distance for GRI-3.0 and
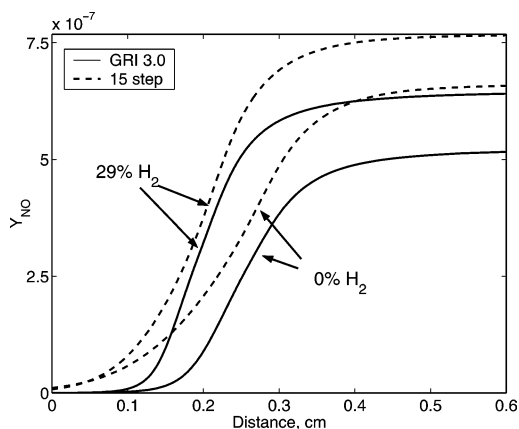15-step mechanism.

Fig. 3. NO mass fraction versus distance for GRI-3.0 and
15-step mechanism.

mismatch may be the steady-state assumptions for N_2O and NO_2, particularly early in the flame. However, use of that mechanism would incur an additional computational expense that was considered unnecessary here, where a qualitative trend is sought. For higher pressure conditions it may be necessary to re-examine this issue.

4. Surface-based postprocessing

In order to better understand the simulation results, surface-based postprocessing of the data was conducted. In this approach, the flame is identified with an isoscalar surface and statistics are extracted from that surface. Here the surface is taken as a methane mass fraction isosurface, where the isolevel considered corresponds to the maximum-heat-release-rate location in the freely propagating laminar flame. The surface is extracted by a triangulation method, and various statistics are interpolated to the surface points. These include the flame curvature, $\nabla \cdot \mathbf{n}$, and tangential flame strain,

$$a_t = (\delta_{ij} - \mathbf{n}_i \mathbf{n}_j) \frac{\partial u_i}{\partial x_j}, \tag{1}$$

where δ_{ij} is the Kronecker delta function, $\mathbf{n}$ is the flame normal direction defined as pointing to the reactants, and $\partial u_i / \partial x_j$ is the flow-velocity gradient. Also extracted are the unweighted and density-weighted flame displacement speeds s_d and s_d^* defined for a species α as [42]

$$s_d = \frac{\omega_\alpha + \frac{\partial}{\partial x_i} D_\alpha \rho \frac{\partial Y_\alpha}{\partial x_i}}{\rho |\nabla Y_\alpha|}, \tag{2}$$

$$s_d^* = \frac{\rho}{\rho_0} s_d, \tag{3}$$

where ω_α is the species reaction rate, D_α is the diffusivity, ρ is the density, ρ_0 is the fresh gas density, and Y_α is the species mass fraction.

In the postprocessing analysis, reference will be made to the turbulent flame speed s_t. Here this is defined based on the rate of methane consumption as

$$s_t = \frac{1}{\rho_0 Y_0 L_y} \iint \omega_{CH_4} \, dA, \tag{4}$$

where Y_0 is the CH_4 mass fraction, and the integration is taken over the entire two-dimensional domain. The flame turbulent speed can be decomposed into contributions from the flame area, A, the laminar flame speed, and a factor I_0 accounting for turbulent influences on the burning rate per unit area [27]:

$$s_t = s_L I_0 A. \tag{5}$$

The evolution of flame area is governed by the competition between the tangential strain a_t, which tends to produce flame area, and the stretch due to curvature, $s_d \nabla \cdot \mathbf{n}$, which on average tends to destroy flame area [24]. Therefore the dependence of the displacement speed on curvature is crucial in determining the overall rate of change of area, and hence also controls the diffusive-thermal stability.

In addition, various statistics are extracted from lines in the directions normal to the surface. These include reaction rates and heat release integrated along the normal directions and maxima and minima along the normal directions of various quantities such as species mass fractions, temperature, and reaction rates. In forming these statistics, care must be taken to gather only statistics corresponding to the local flame element. Since the flame is wrinkled, the normal can cross multiple flame elements. This problem is circumvented here by defining start and end points for the normal that ensure that the scalar defining the isosurface (the methane mass fraction) remains monotonic.

5. Qualitative comparison with experiment

Here a qualitative comparison is made with the experiments of [17]. It should be emphasized at this point that the DNS cannot quantitatively reproduce the experimental conditions, where phenomena such as large scale shear, recirculation and heat losses are important. Nevertheless the comparison is useful to gain a qualitative understanding of the differences between the pure methane and enriched flames.

Fig. 4 shows the OH mass fraction field for Cases A (0% H_2, on the left) and B (29% H_2, on the right), respectively. (Results here pertain to a snapshot at two eddy turnover times into the simulation.) A methane isosurface corresponding closely to the location of maximum heat release is also shown. The flame propagates from right to left. These may be compared with Fig. 5, which shows OH planar laser induced fluorescence (PLIF) images for the same mixtures taken from the experiments of [17]. It may be observed that the experimental and DNS images show some qualitative similarities. The levels of OH are substantially higher, in general, in the enriched flame, with peaks occurring in structures that protrude into the reactant side. Wrinkling scales are comparable between DNS and experiment for the pure methane case, the large scales being on the order of 1 to 5 mm (in fact, the integral scale used for the simulations was deduced from OH PLIF images such as these). It may be observed that the experimental images for the enriched flame show a much more wrinkled structure than the pure methane flame. The same trend is observed in the simulated images, but is not as pronounced. A speculative explanation could be that the
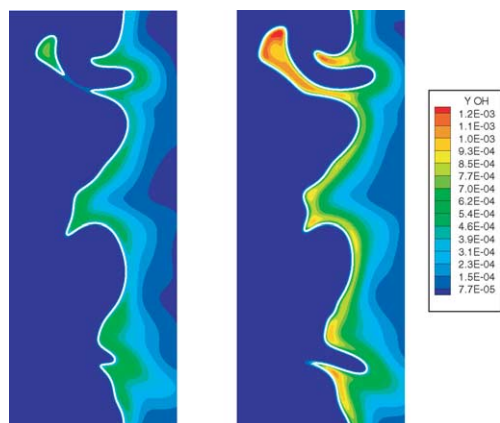
Fig. 4. OH mass fraction field (color scale) and CH$_4$ contour (white line): left, Case A, 0% H$_2$; right, Case B, 29% H$_2$; dimensions: 1.2 by 3.0 cm.
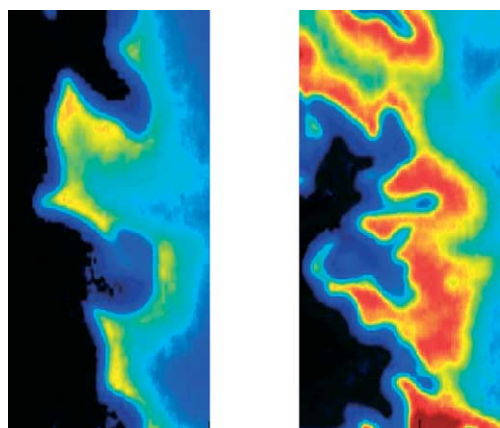

Fig. 5. OH PLIF signal [17]: left, Case A, 0% H$_2$; right, Case B, 29% H$_2$; dimensions: 1.5 by 3.0 cm.

experiment represents a statistically stationary flow in which thermal-diffusive effects on the flame structure are fully developed, whereas the calculation represents a developing flame. Also, the flow field in the burner is not homogeneous—the greater resistance of the enriched flame to turbulence may allow it to penetrate areas of higher u' in the burner, leading to a more wrinkled flame.

Although not shown in Fig. 5, it is observed in the experiments [17] that the pure methane flame has a more broken structure with areas of local extinction under these conditions. In the DNS, an extinction event, the pinchoff a pocket of reacting material is observed for the methane case but not for the H$_2$-enriched case. This extinction event is analogous to extinction in a symmetric opposed jet flame. Other kinds of extinction, such as flame detachment from the bluff body, cannot be represented in the present simulations of a freely propagating flame. Extinction

due to the lean limit could have been observed but did not occur in the simulations.

6. Flame stability

Here the turbulent flame speed is taken as a measure of flame stability in the lean blow-off limit. A higher turbulent flame speed may allow the enriched flame to better resist flame blow-off. In this section, the flame area and flame structure contributions to the turbulent flame speed are quantified for the pure methane–air and the hydrogen-enriched methane–air flame. The influence of intrinsic diffusive-thermal effects on the curvature stretch and thus the overall burning rate is discussed.

The turbulent flame speed defined based on the integrated methane consumption rate in the computational domain is plotted versus simulation time in Fig. 6. It is readily observed that the turbulent flame speed for the enriched flame is substantially higher than that of the pure methane flame. At two eddy turnover times (2 ms), it is a factor of 2.2 higher. This may be somewhat surprising, as the enriched laminar flame only propagates at a rate 1.4 times that of the CH$_4$ flame. The increase in volumetric heat release rate is due to three principal contributions. First, as previously mentioned, the laminar flame propagates faster in the enriched case, second, more area is generated (a factor of 1.3), and third, turbulent stretch affects the local structure (a factor of 1.2). Thus under these conditions the three components have roughly equal contributions. It is instructive to examine in more detail the area and local structure contributions.

Fig. 7 shows the total flame length versus simulation time. It is seen that the enriched flame develops flame area faster than the pure methane flame, and this contributes to a higher turbulent flame speed. Since the enriched laminar flame propagates faster, it might be expected that in fact less area would be generated owing to the greater rate of flame-surface-area consumption due to the combined effect of propagation and curvature (see for example [24]). Additionally, the residence time of the flame in areas of positive strain is reduced for faster propagation speeds, reducing the net stretch effect [43]. However, these arguments neglect to consider the thermal-diffusive effects on the displacement speed and quenching events due to flame annihilation. Plotted in Fig. 8 are the area-weighted flame strain and flame stretch due to curvature ($s_d \nabla \cdot \mathbf{n}$). The negative stretch rate due to the combined effect of propagation and curvature is generally more for the pure methane case than for the enriched flame. This is due to an effect of a diffusive-thermal nature that will be discussed later.
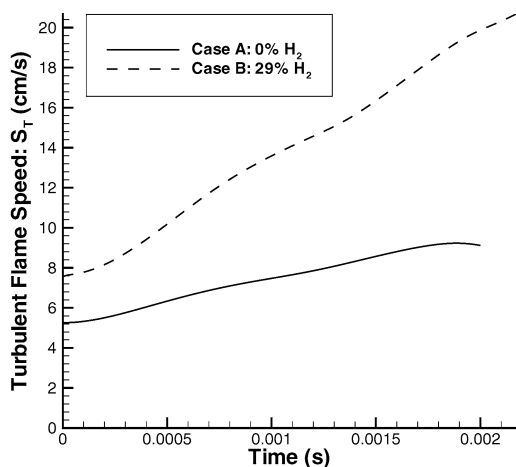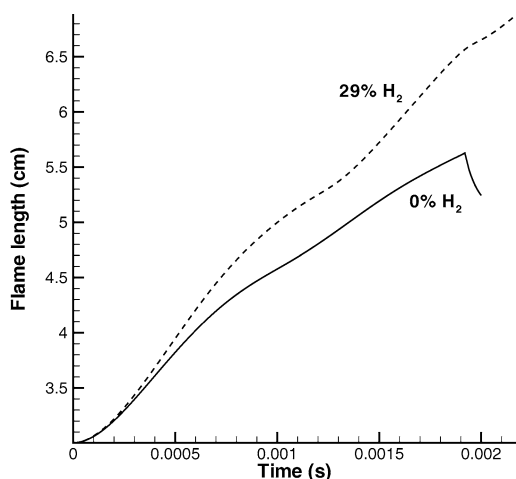
Fig. 6. Turbulent flame speed versus time.

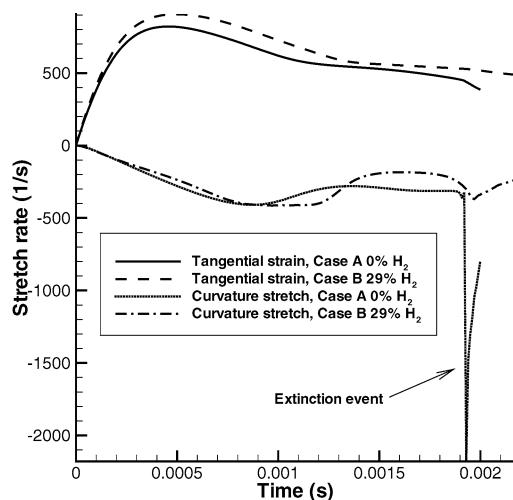Fig. 7. Flame length versus time.

Fig. 8. Flame strain and curvature stretch versus time.
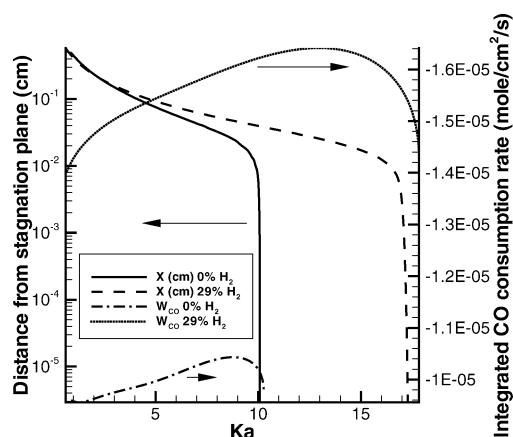

Fig. 9. Integrated CO consumption reactions and distance of maximum CO consumption from stagnation plane versus Karlovitz number. Extinction in twin-flame configuration occurs soon after the CO oxidation layer merges with stagnation plane.

In addition it may be noted that a large negative spike exists in the curvature stretch in Fig. 8 for Case A, but not for Case B. This can also be observed in the near-discontinuity in the slope of the flame length curve (Fig. 7). It is due to an annihilation event (in this case the pinchoff of a pocket of reacting material) arising from downstream interaction. (The detached pocket of reacting material may be observed for the methane case in Fig. 4.) This points to an important difference between the two flames—the resistance to extinction by downstream flame interaction. The term downstream interaction relates to the flame topology and refers to the situation in which the burnt-gas side of the flame element is sufficiently close to the burnt-gas side of another flame element so that the two interact—for example, as in a flame pushed near to the stagnation plane in a symmetric opposed jet flow. Steady laminar calculations in the symmetric opposed jet configuration reveal that the extinction

strain rate for the pure-methane case is $326 \ s^{-1}$, compared with $1061 \ s^{-1}$ for the enriched flame. Extinction for these mixtures occurs due to incomplete reaction when the flames are pushed against the stagnation plane. A closer analysis reveals that extinction occurs soon after the CO oxidation layer of one flame merges with that of the twin flame. This may be seen in Fig. 9, showing the integrated CO consumption rate and the distance of its maximum point from the stagnation plane against the Karlovitz number (Ka), defined as $a_t \tau_{th}$. The reason for the large difference in extinction strain rates appears to be timescale-related. The unstrained thermal timescale of the enriched flame is approximately half that of the methane flame. As the strain is increased, the timescale decreases for both
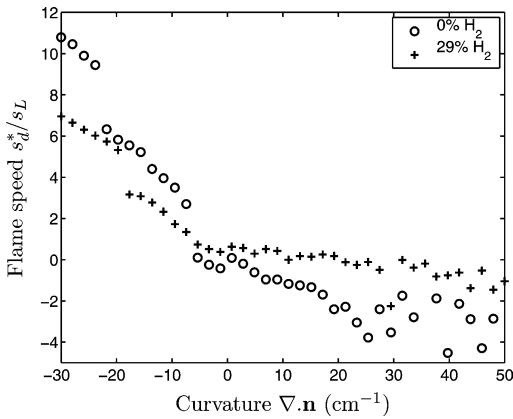
Fig. 10. Density-weighted displacement speed versus curvature (1/cm). Curvature mean is near zero in both cases: 1.9 for Case A, 0.8 for Case B. Curvature RMS is 18.4 for Case A, 13.3 for Case B.

Fig. 11. Methane consumption rate and hydrogen mass fraction at the flame surface normalized by the laminar values versus curvature.

flames due to the Lewis-number effect (the effective Lewis number is less than one for methane flames at this equivalence ratio), but not as rapidly as the strain timescale, leading to eventual extinction. If the change in flame timescale with strain is accounted for, extinction occurs at nearly the same Karlovitz number for both flames (4.8 for Case A and 4.6 for Case B).

A final observation should be drawn from Fig. 8— that the strain experienced in the case of the enriched flame is greater than that in the case of the pure methane flame. This is because the enriched flame survives better in areas of high strain.

To investigate further the reason for the difference in the curvature contribution to the flame stretch rates, the density-weighted flame speed, s_d^*, is plotted against curvature in Fig. 10. This plot relates to a single time-snapshot of the simulation, at two eddy turnover times. All other single-time results presented in this paper relate to this instant. Averaging over intervals of curvature has been performed to reduce data scatter. The qualitative trend is not sensitive to the interval used. Note that using the convention adopted here, positive curvatures have the center of curvature in the products. It is evident that curvature and flame speed are negatively correlated for both cases, consistent with the behavior of a thermal-diffusively stable flame. In this situation, positively curved elements, which produce area when they propagate (with positive speeds), have a lower flame speed than negatively curved elements, which destroy flame area, leading to a net stabilizing influence. The slope for the H_2-enriched flame is less, indicating it is less stable. In part this is due simply to the thinner flame structure— a thinner flame can tolerate finer-scale wrinkling. Also, there is an effect associated with the diffusivity of H_2, which is preferentially focused into areas with
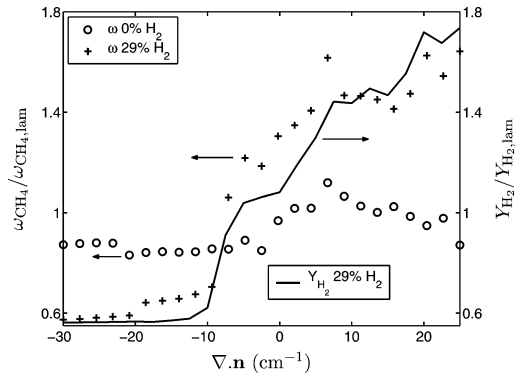
positive curvature, and preferentially defocused from areas of negative curvature. It should be noted that at larger levels of H_2, a diffusive-thermally unstable flame could result; however, such a large proportion of hydrogen is unlikely to be practical from an economic standpoint.

The preferential diffusion of hydrogen at positive cusps is revealed by a plot of the CH_4 reaction rate and the H_2 mass fraction (for the enriched case) evaluated at the flame surface against curvature in Fig. 11. Recall that the reaction rate is directly related to the displacement speed through Eq. (3). Considering the CH_4 reaction rate, no trend is discernible for the pure-methane case, but the reaction rate is seen to be positively correlated with curvature for the enriched case. The positive correlation is due to focusing of H_2 into positively curved elements, which may be verified by observing the positive correlation of H_2 mass fraction with curvature. The fuel species are focused into these elements and this competes with the defocusing of heat. In the case of the pure methane flame, little correlation is observed, because methane has roughly the same diffusivity as heat. However, H_2 is a smaller and more diffusive molecule, leading to a net increase of the local equivalence ratio and more intense burning in the enriched flame.

Referring again to Fig. 10, particular note is made of the negative flame speeds found for positive curvatures, predominantly in the methane case. Since these occur at large positive cusps, large negative curvature stretch results and there is a significant reduction to the total balance of flame area production. Indeed the total stretch for the pure methane case is negative at this instant (at two eddy turnover times). By contrast, the total stretch is positive for the enriched case. The large negative speeds are due to highly transient extinction events caused by flame–flame interaction and the high local curvatures that result, for example as pointed out in reference to Fig. 8. This supports the
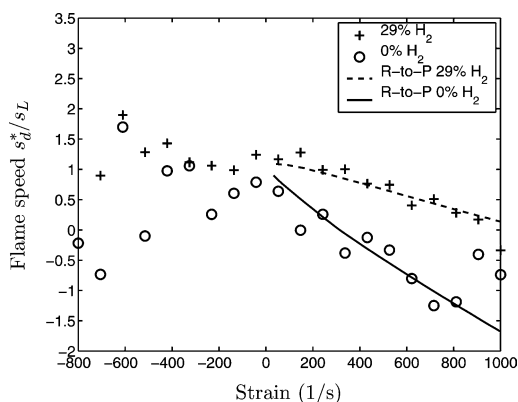
Fig. 12. Density-weighted displacement speed versus strain: top, Case A; bottom, Case B. Symbols: DNS data; lines: laminar opposed jet calculation in reactant-to-product configuration.
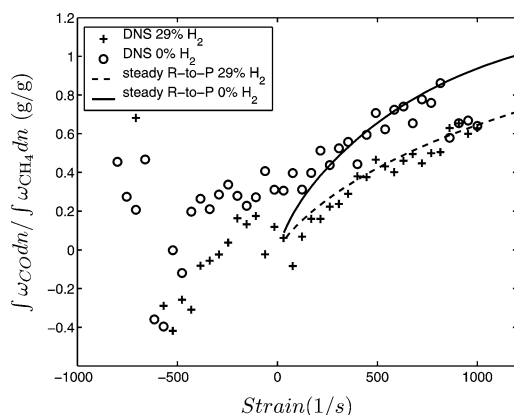

Fig. 13. Integrated CO net production rate over CH_4 net consumption rate versus strain. Symbols: DNS data; lines: laminar reactant-to-product configuration.

conjecture of [9] that the resistance to extinction is an important factor in understanding the effects of H_2 enrichment on stability.

Earlier it was stated that the increase in the turbulent flame speed was greater in the enriched case for three reasons—the faster laminar burning rate, the greater area, and a mean effect of the turbulence on the local structure leading to a different burning rate per unit area. In order to investigate the last reason, the density-weighted displacement speed is plotted against tangential strain in Fig. 12. Averaging over intervals of strain has been performed to reduce data scatter. Qualitative results are insensitive to the size of the intervals.

It is seen that for positive strains, both cases show a diffusive-thermally stable behavior, as was observed in the plot against curvature, Fig. 10. It is observed that the slopes of the two lines are different—the pure methane flame is more sensitive to strain. The qualitative trend matches the laminar calculations, despite the strong unsteadiness. In part the difference in slope is due to the difference in flame timescales—the enriched flame has a shorter timescale and thus is less affected for the same strain. Also, there is a diffusive-thermal effect due to the preferential diffusion of H_2 into the flame. Since the mean strain is positive, this leads to a net reduction in the flame speed with respect to the enriched flame, and would be represented in Eq. (5) by a reduced value of I_0. This analysis is consistent with previous DNS results using simple chemistry [24,44], where $Le < 1$ flames are found to have a higher average flame speed than $Le \geqslant 1$ flames, and with complex chemistry [42,45–47], where the average flame speed is dependent on equivalence ratio.

While curvature has been shown to affect the local flame speed more strongly than strain [44] in simple

chemistry calculations, the effects were found to average out in the mean, since the trend of curvature with flame speed was nearly linear, and curvature had nearly zero mean. However, in the present simulations, a net effect may be present due to the nonlinearity of the flame speed–curvature correlation. It is observed in Fig. 10 that this correlation is nonlinear, with the slope in positive curvature regions being less than that in negative curvature regions. This fundamental distinction between positive and negative cusps is associated with chemical nonlinearity and has been pointed out previously by [22]. Thus even for a symmetric curvature distribution with zero mean, a net influence of curvature can result, in contrast to simple chemistry calculations where there is typically a more linear flame speed–curvature correlation. Since the bending associated with positively curved flame elements is less for the pure methane case than the enriched case, a net relative increase of flame speed may be seen. The difference is attributed to the focusing of H_2 into the flame, and the enhanced chemical response that results.

7. CO emissions

Higher emissions of CO are an undesirable product of methane combustion near the lean stability limit. One of the main reasons for the addition of H_2 is to reduce these emissions. Previous experimental studies have found reduced CO emissions (e.g., [17]), but steady flame computations have not yet adequately explained the observed reductions.

In the DNS, roughly a 20% reduction is observed in CO production rate per unit methane consumption for the enriched case, a trend which is consistent with previous experimental observations. This may be observed in Fig. 13, showing the CO production

rate integrated in the flame-normal direction per unit methane consumption rate, also integrated in the normal direction, against the flame strain. The same value for the steady strained computation in the reactant-to-product configuration is also plotted for comparison. It may be seen that for the enriched case, the CO produced is universally lower across all strain rates.

In this section the reduction in CO for the enriched flame is explained in terms of two effects—strain and the degree of interaction with other flame elements. Multidimensional and unsteady influences are highlighted. Lower CO emissions are shown to occur in the enriched flame due to a faster flame timescale for flame elements that are positively strained and relatively free of downstream interaction. Elements undergoing downstream interaction (both positively and negatively strained) are shown to be responsible for the majority of CO production, and in the enriched case, less CO is produced due to locally faster CO oxidation timescales in these regions. The extent to which the CO behavior in the turbulent flame is captured by simple one-dimensional laminar steady strained flames is determined.

For positively strained flame elements, where curvatures tend to be low and there is generally little downstream interaction, the reduction in CO levels for the enriched flame is timescale related. When plotted against Karlovitz number, i.e., accounting for the faster chemical timescale in the enriched case, the curves of Fig. 13 are almost identical in the positive-strain region. The reason for this similarity is that the reaction path leading to CO production does not change, only the overall rate. While the CO oxidation rate increases with strain faster for the enriched case, CO production does so as well. The principal oxidation step for CO, $CO + OH \Leftrightarrow CO_2 + H$, increases with OH concentration. The OH concentration increases with strain owing to the $Le < 1$ behavior, which accelerates the breakdown of methane and the formation of CO. This result is consistent with the observation of [18] that the CO reaction path was insensitive to hydrogen blending.

It may also be observed in Fig. 13 that, in the positive-strain region, the steady laminar reactant-to-product model gives qualitative agreement with the DNS results for both cases, validating the use of these models to provide understanding in the positive-strain region. This is very surprising given the level of unsteadiness encountered by these flames. For comparison, the same data are shown without averaging over intervals of strain for the pure-methane case in Fig. 14. The large data scatter is evident and is due to effects of curvature and unsteadiness. An interesting point is that these effects tend to average away in the mean, leaving a trend that is close to the laminar model. It has been shown in theory [20] and compu-
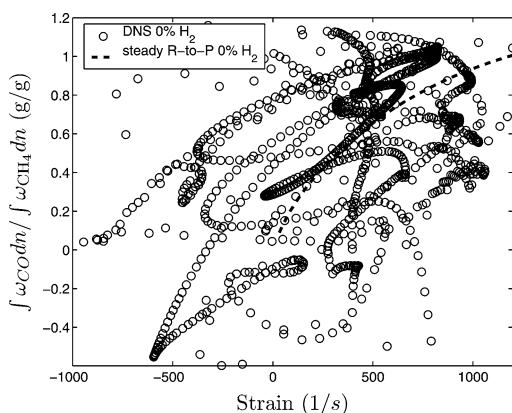

Fig. 14. Integrated CO net production rate over CH_4 net consumption rate versus strain. Symbols: DNS data; lines: laminar R-to-P configuration.

tations [21] that Markstein effects vanish for larger frequencies—i.e., that the curve of the flame response to strain tends to have a zero slope. However, these analyses considered only a single flame. When an average is taken over many flame elements subjected to unsteady strain in different phases, a result closer to the laminar flame predictions may be found. This interesting result deserves further investigation, and will be addressed in future work.

In Fig. 13 a different trend is observed between positive- and negative-strain regions. In the negative-strain region, CO production tends to be higher than predicted by extrapolation of the positive-strain trend into the negative-strain region. This is particularly true in the case of the pure methane flame. The different trend for compressive strain regions can be explained by analyzing the surface data accounting for the effect of downstream interaction, as outlined below.

It is observed in the simulations that qualitatively different behavior with regards to CO is found in flames undergoing a downstream interaction and those that are not. In a highly wrinkled flame such as in the present situation these interacting regions coincide with positive cusps and the "wings" adjacent to the positive cusps, where the approximation of a flame as an isolated one-dimensional element breaks down. A postprocessing analysis was developed that is able to distinguish between interacting and noninteracting flames. The criteria for flagging an interacting flame element are based on the normal distance of that element from another element (defined based on the monotonicity of the isosurface scalar). If this distance is less than a characteristic distance on the order of the thermal flame thickness, or the radius of curvature is positive and less than the characteristic distance, an interacting flame is flagged. Tests were performed on the sensitivity of the results to the
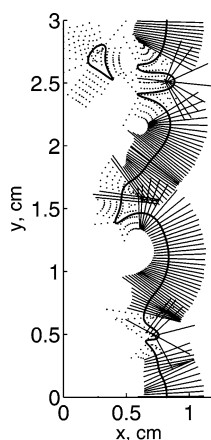
Fig. 15. Case A methane contour (thick black line) and normal directions divided into interacting (dotted lines) and noninteracting (solid lines) elements. (Only a fraction of the elements are shown.)

distance used for flagging interaction, and while it is found that the area of the flame flagged as interacting is dependent on the distance used, use of a distance on the order of the thermal thickness was effective for dividing the flame into qualitatively different behaviors.

Fig. 15 shows an example of the division of a subset of the flame normals into interacting and noninteracting flames. In this example the thermal flame thickness is chosen to be the characteristic distance to distinguish between interacting and noninteracting flames. The solid lines are classified as noninteracting, and in these areas the most appropriate strained laminar flame model is suggested to be the reactant-to-product configuration (R-to-P), in which one nozzle supplies fresh reactants and the other supplies products of combustion. In this configuration, a single flame is observed between the nozzles, and for a sufficiently diffusive fuel, increasing the flowrate through the nozzles eventually causes the flame to cross the stagnation plane, where a negative displacement speed may be observed [48]. In the case of the interacting flames, the dotted lines in Fig. 15, the symmetric twin-flame model may be more appropriate. In this situation, both nozzles supply reactants and two flames are observed. Increasing the flow rate for the mixtures considered eventually causes the flame to be pushed against the stagnation plane and extinguished—clearly a steady negative displacement speed cannot be observed.

The flames were separated into interacting and noninteracting regions as described, using the distance $\delta_{th}/2$ to flag an interacting element. Figs. 16 and 17 show the data as in Fig. 13 for Cases A and B, respectively, but separated into interacting and noninteracting flame elements. Results from the laminar R-
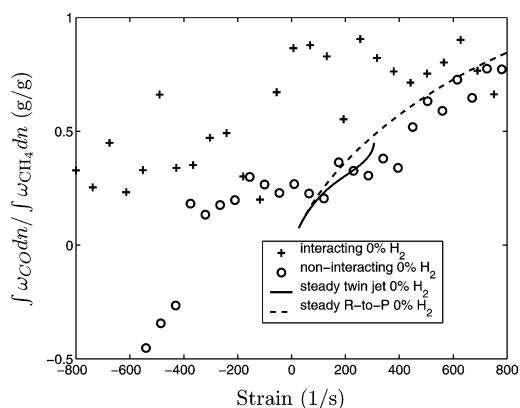

Fig. 16. Integrated CO net production rate over CH_4 net consumption rate versus strain, separated into interacting and noninteracting zones. Symbols: DNS data; lines: laminar calculations.
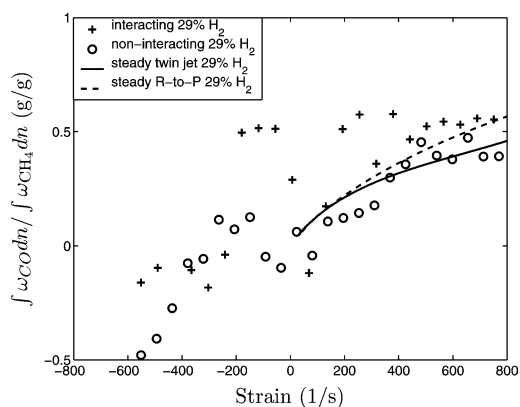

Fig. 17. Integrated CO net production rate over CH_4 net consumption rate versus strain, separated into interacting and noninteracting zones. Symbols: DNS data; lines: laminar calculations.

to-P and twin-flame configurations are also plotted for comparison. It is readily observed that in both cases the CO production rate per unit methane consumption is generally higher for the interacting flames than for the flame elements free of downstream interaction. This effect can be explained by an unsteady downstream interaction (leading to local extinction in some cases). The CO oxidation layer is found toward the downstream portion of the flame and is therefore the first to be annihilated as downstream flame–flame interaction proceeds. However, the CO production layer is closer to the fresh gas side of the flame and remains active longer in a downstream interaction. Thus, when CO production is left active, but CO consumption is quenched in a downstream interaction, a higher net rate of change of CO is observed. This is highlighted in Fig. 18, showing contours of CO levels in solid lines and OH contours as thick dashed lines, OH be-
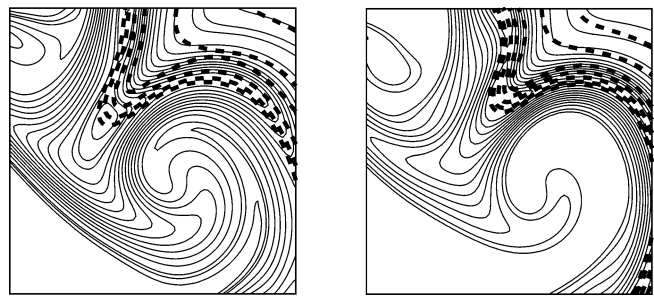
Fig. 18. Quenching of CO oxidation layer in downstream interaction. CO mass fraction contours (thin solid lines), OH mass fraction contours (thick dashed lines). Left: 0% H_2, right: 29% H_2.

ing responsible for most of the CO oxidation. For this positively curved region, the CO oxidation layer is pinched off; however, the CO production layer is less affected, resulting in the observed higher CO levels at the end of the positive cusp. Because the hydrogen-enriched flame has a faster timescale overall, and in particular a faster CO oxidation timescale (due to higher OH levels and higher temperature), it is much more resistant to downstream interaction and extinction. (Note in Fig. 18 the greater penetration of OH into the area of higher CO due to multidimensional effects in the cusp vicinity.) Under a given level of downstream interaction, which is supported by the local strain field, the enriched flame responds faster to that level of strain, allowing the CO oxidation to proceed closer to completion. This may be observed more quantitatively by comparing CO production per methane consumption in Figs. 16 and 17. Although the same qualitative trend is observed for both cases, it is clear that incomplete oxidation of CO is much more pronounced for pure methane.

The transient character of annihilation events coupled with multidimensional effects locally is highlighted by the inability of the one-dimensional laminar models to capture the qualitative trend for interacting flames (Figs. 16 and 17), even using the twin-flame model, which captures steady downstream interaction. This helps to understand the reason that steady-flame models have failed [18] to predict the practically observed trend of CO with H_2.

Some quantitative information was also extracted to determine the overall contribution of downstream interaction to CO production. Using the reaction rates along flame normals, it is possible to obtain quantitative estimates of how much CO is produced in areas of downstream interaction. For a thin flame that is not significantly curved, it is possible to use the following approximation for the domain integrated reaction rate,

$$\iint \omega_\alpha \, dA \approx \left\langle \int \omega_\alpha \, dn \right\rangle_s L, \qquad (6)$$

Table 4
Statistics obtained for CO emissions (distance $= \delta_{th}/2$)

Statistic	0% H_2	29% H_2
% flame area interacting	43	39
% CO produced in interacting areas	81	72
% error on total CO produced using Eq. (7)	5	9
$\iiint \omega_{CO} \, dV / \iiint \omega_{CH_4} \, dV$ for interacting areas (g/g)	0.8	0.65

where $\langle \ \rangle_s$ denotes a flame length-weighted surface average, and L is the flame length. However, here a first-order method of accounting for the effects of curvature is used. The usual integral along the flame normal is replaced by an expression accounting for the curvature, essentially an integration over a segment of a circle,

$$\iint \omega_\alpha \, dA \approx \left\langle \int \omega_\alpha (1 + n\nabla \cdot \mathbf{n}) \, dn \right\rangle_s L, \qquad (7)$$

where the integration is terminated when $1 + n\nabla \cdot \mathbf{n} = 0$.

The data obtained using this estimate are reported in Table 4. A distance of $\delta_{th}/2$ is used to flag an interacting flame. The flames have approximately the same fraction of area undergoing interaction, with the pure methane flame showing slightly more interaction, perhaps due to the larger flame thickness. It is seen that the CO is produced mainly in the interacting areas for both cases. The pure methane case shows slightly more CO production in interacting flames. A difference is observed in the CO produced per unit methane consumed in the interacting flame areas, with the enriched flame producing less CO owing to the higher concentration of OH and higher temperatures that are observed in the interacting areas (see Fig. 4), allowing oxidation of CO to complete before the downstream interaction.
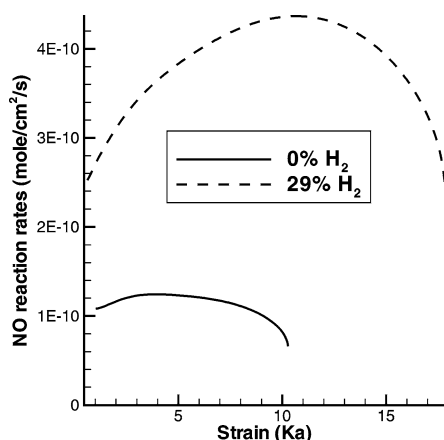
Fig. 19. Integrated NO reaction rate versus strain (Karlovitz number) for steady opposed twin jet flame.

Fig. 20. Mean NO reaction rate versus time in DNS.

8. NO emissions

Owing to the higher combustion temperatures and higher radical concentrations, the addition of H_2 might be expected to have a negative impact on NO_x emissions. In the present simulations, this is observed. Relative to the pure methane flame, there is roughly a 50% increase in the mass rate of NO production per unit heat release. In the experiments of [17] no negative impact on NO was observed. However, it should be noted that in those experiments, a large difference in NO levels between pure methane and the enriched flames was noted near the center body, but similar levels were found downstream. A timescale as long as the convective time to the downstream measurement location is presently not accessible to DNS. This simulation may be more applicable to the region near the center body, where qualitative agreement with the experimental trend is found.

For the equivalence ratio considered here, combustion temperatures are very low (with a maximum of 1540 K), and in fact the NO levels are very low for both flames, less than one part per million, so the increase observed here may not be an important practical consideration. In addition, for these simulations the overall equivalence ratio was fixed. In practice, H_2 addition may allow combustion at overall leaner equivalence ratios, and thus lower temperatures, leading to lower NO_x emissions.

Despite the low NO levels, it is instructive to examine where the increase arises from, considering that in the freely propagating flame there is only a 16% difference in the NO production rate per unit heat release. Results for the integrated NO reaction rates in the strained laminar twin-flame configuration are presented in Fig. 19. The NO formation system in these flames involves many reactions, with large positive and negative contributions from various paths.
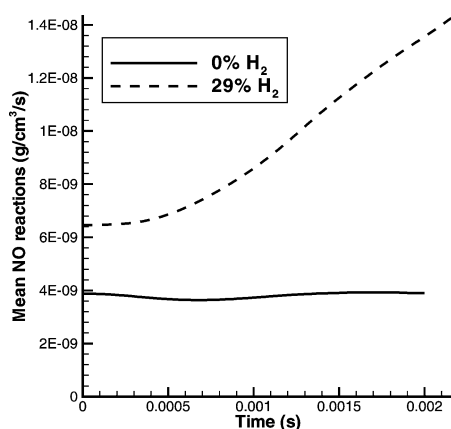
A reaction-path analysis was performed and indicated that under these very lean conditions, reaction paths involving the species NH, NNH, N_2O, and HNO, along with the well-known thermal Zeldovich reactions involving N, were all significant, and of roughly equal magnitude. The flame has $Le < 1$ behavior and temperature and radical concentrations increase with strain until a turning point, after which they decrease until extinction. The integrated NO reaction rate follows the trend of radical concentrations and temperature. The reaction-path analysis showed that all identified reaction paths followed the same trend with strain, except for the N_2O path, which began to decrease with strain much earlier than the other paths. It is clear that the enriched flame shows a greater influence of strain on the net NO production rate. This is because the enriched fuel is more diffusive, leading to greater increases of radical concentrations and temperatures with strain. In turn, these increase the rates of the NO formation reactions. However, there was no major change in the overall reaction path with respect to the hydrogen addition, although routes involving NH and NNH were enhanced to a greater degree by strain in the enriched case.

In Fig. 20, mean NO reaction rates are shown for the DNS simulations. The reaction rates are presented as a mean in the domain versus time. It is seen that behavior is qualitatively similar between the DNS simulation and the steady laminar flame. In the DNS, the enriched flame shows an increase with time (as the flame is progressively strained), whereas the pure methane flame shows essentially no change.

Fig. 21 shows contours of the local NO reaction rate for both cases on the same scale. The NO reaction rate is universally higher in the enriched flame. For both flames, NO peaks in areas of positive curvature or downstream interaction, where radical concentrations are higher. The peaks are more pronounced for the enriched flame because of the focusing of the H_2
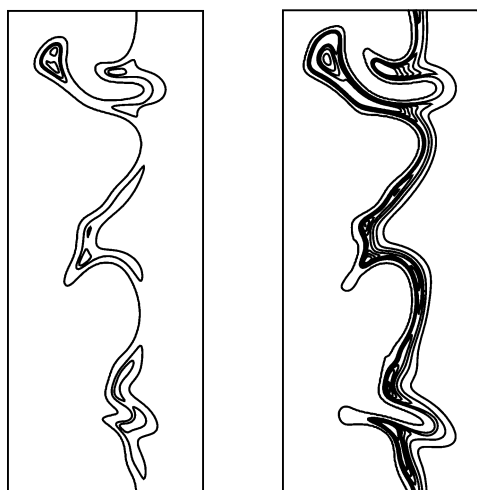
Fig. 21. Contours of NO reaction rate (1/s). Left: 0% H_2; right: 29% H_2. The maximum NO reaction rate is 4.5 times greater in the 29% H_2 case.
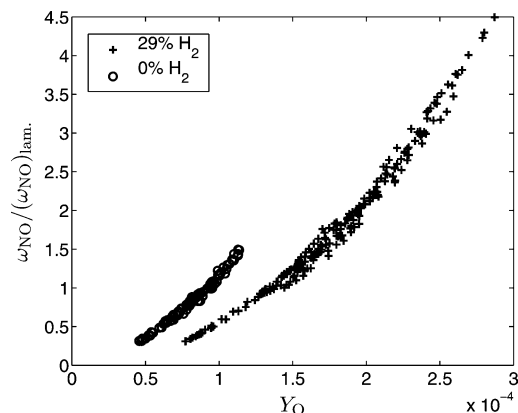

Fig. 22. Local NO reaction rate normalized by the laminar value versus O radical mass fraction.

fuel into the flame, leading to locally richer mixtures and thus higher radical concentrations and temperature. As further evidence that radical levels are important, NO reaction rate evaluated at the flame surface is plotted against the O radical mass fraction in Fig. 22. The plot shows a remarkably good correlation for both cases. Note that data averaging over intervals of Y_O has not been performed for this figure. Similar correlations are observed for OH and other radicals of the hydrogen combustion subsystem. A similar trend is seen for the two cases, but it is extended much further in the enriched case due to locally high levels of O radicals. The integrated NO reaction rate along the flame normal is shown in Fig. 23 versus the maximum temperature along the normal. A positive correlation is observed for both cases, and again the correlation is simply extended for the enriched case owing to the
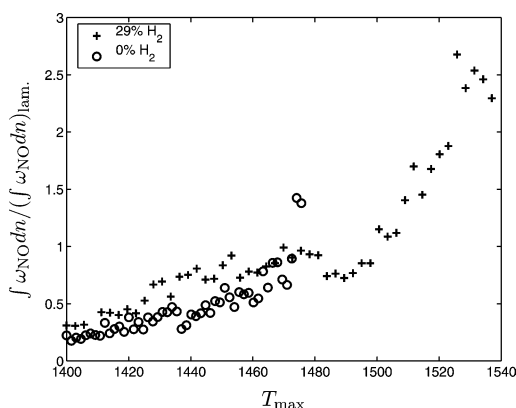

Fig. 23. Integrated NO reaction rate normalized by the laminar value against maximum temperature along the normal.

focusing of H_2 creating zones of higher temperature. A reaction path analysis did not reveal any significant change of reaction pathways in the DNS compared with the one-dimensional strained calculations.

While the NO levels observed in these simulations was quite small, it is very likely that similar effects could be observed for richer conditions that produce more NO. The same H_2 focusing mechanism would still be active, resulting in regions of higher NO production.

9. Conclusions

Direct numerical simulation has been used to study the effects of H_2 enrichment on lean premixed methane–air flames. A numerical experiment was conducted in which two flames having different fuel mixtures were subjected to initially identical two-dimensional random flow fields. The differences between the flames were studied to help understand the possible effects of H_2 enrichment on flame stability and pollutant formation.

Flame stability was examined from the perspective of the turbulent flame speed. A higher turbulent flame speed may promote a greater resistance to flame blow-off and thus a more stable flame. In the present work, a higher turbulent flame speed was observed for the enriched flame, which is consistent with enhanced blow-off stability observed in experiments [17]. This was attributed to a higher laminar flame speed, a greater flame surface area, and a greater burning rate per unit area. The larger flame surface area arises from the influence of focusing of H_2 into the flame and a shorter flame time-scale. These factors were found to lead to an enriched flame that is less thermal-diffusively stable and more resistant to extinction than the pure methane flame, resulting in a greater total flame area generation. For the enriched flame, pref-

erential diffusion of H_2 into positively curved and strained elements results in locally richer regions and a net increase in the burning rate per unit surface area. Further work is needed to understand the quantitative effect of H_2 addition in a real burner environment, where simply exhibiting a higher flame speed is not the complete picture with regard to stability.

Emissions of CO were investigated. Lower CO emissions per unit methane consumption were found in the enriched flame, consistent with previous experimental studies. Emissions of CO were found to be produced mainly in areas of the flame undergoing downstream interaction, where the CO oxidation layer is curtailed. Downstream interaction is caused by the local strain field, and the influence of this is less in the enriched case due to the faster CO oxidation timescale brought about by higher radical concentrations that occur locally. CO production was found to be fundamentally unsteady in areas of downstream interaction, since flames undergoing downstream interaction are sensitive to extinction. Since downstream interactions generally coincide with regions near positive cusps, and radical enhancement due to preferential diffusion of hydrogen at the cusp has a large region of influence, multidimensional simulations are required to capture CO emissions. This may be why steady one-dimensional calculations have not explained the practically observed trends of CO emissions with H_2 blending. Further work is needed to understand CO emissions in a practical setting, for example, where heat losses and mixing with cooler coflowing air might have a large influence on local quenching and thus CO emissions.

Emissions of NO were also studied. A 50% increase in NO production per unit heat release was observed for the enriched flame relative to the pure methane flame. This was attributed to locally high temperatures and radical levels, brought about by the focusing of H_2 into flame elements protruding into reactants. The increase indicates that practically there may be a tradeoff between NO and CO emissions with regard to H_2 enrichment. However, the levels observed in the present simulations were very low because of the low equivalence ratio chosen for this study, so this increase may not be of practical significance. Also, in the present numerical experiment, the equivalence ratio was fixed, but in a practical scenario, H_2 blending may allow burning at lower equivalence ratios, reducing flame temperatures and thus NO. Finally, in the gas turbine application, it is likely that higher temperatures and certainly higher pressures would be encountered, which would significantly change the NO formation pathways, with the more traditional thermal and N_2O paths becoming dominant over the other paths discussed here. In this case it can be predicted that, even for two mixtures with the same adiabatic flame temperature, slightly higher NO levels may be observed in the enriched flame due to the focusing of H_2 resulting in zones of locally higher radical concentrations, and possible "super equilibrium O" NO formation through the thermal mechanism [1]. The importance of these zones clearly depends on their size relative to the zones of a more homogeneous mixture. It is suggested that one-dimensional strained flame calculations could be used to study the effects of pressure and temperature since the qualitative trend of NO with H_2 blending seen in present simulations was also observed in steady calculations.

Acknowledgments

References

[1] J. Warnatz, U. Mass, R.W. Dibble, Combustion, Springer, New York, 1996, chap. 17.

[2] S.R. Bell, M. Gupta, Combust. Sci. Technol. 123 (1997) 23–48.

[3] R.M. Clayton, Adv. Chem. Ser. 166 (1978) 267–286.

[4] D.N. Anderson, NASA Technical Memorandum TM X-3301, National Aeronautics and Space Administration, 1975.

[5] J.D. Morris, F.L. Ballard, A. Banti, in: ASME International Gas Turbine and Aeroengine Congress and Exhibition, Stockholm, Sweden, 1998, Paper 98-GT-359.

[6] J.N. Phillips, J.R. Roby, in: ASME International Gas Turbine and Aeroengine Congress and Exhibition, Indianapolis, Indiana, 1999, Paper 99-GT-115.

[7] G. Yu, C.K. Law, C.K. Wu, Combust. Flame 63 (1986) 339–347.

[8] J.L. Gauducheau, B. Denet, G. Searby, Combust. Sci. Technol. 137 (1998) 81–99.

[9] J.-Y. Ren, W. Qin, F.N. Egolfopoulos, T.T. Tsotsis, Combust. Flame 124 (2001) 717–720.

[10] C. Uykur, P.F. Henshaw, D.S.-K. Ting, R.M. Barron, Int. J. Hydrogen Energy 26 (2001) 265–273.

[11] C.J. Sung, Y. Huang, J.A. Eng, Combust. Flame 126 (2001) 1699–1713.

[12] J.-Y. Ren, W. Qin, F.N. Egolfopoulos, H. Mak, T.T. Tsotsis, Chem. Eng. Sci. 56 (2001) 1541–1549.

[13] G.S. Jackson, R. Sai, J.M. Plaia, C.M. Boggs, K.T. Kiger, Combust. Flame 132 (2003) 503–511.

[14] R. Sankaran, H.G. Im, in: Proceedings of the 3rd Joint Meeting of the U.S. Sections of the Combustion Institute, Chicago, Illinois, March 16–19, 2003, The Combustion Institute, Pittsburgh, 2003.

[15] J.M. Plaia, G.S. Jackson, in: Proceedings of the 3rd Joint Meeting of the U.S. Sections of the Combustion Institute, Chicago, Illinois, March 16–19, 2003, The Combustion Institute, Pittsburgh, 2003.

[16] R.W. Schefer, D.M. Wicksall, A.J. Agrawal, in: Proceedings of the 2nd Joint Meeting of the U.S. Sections of the Combustion Institute, Oakland, California, March 25–28, 2001, The Combustion Institute, Pittsburgh, 2001.

[17] R.W. Schefer, D.M. Wicksall, A.J. Agrawal, Proc. Combust. Inst. 29 (2003) 843–851.

[18] C.M. Vagelopoulos, J.C. Oefelein, R.W. Schefer, in: Proceedings of the 3rd Joint Meeting of the U.S. Sections of the Combustion Institute, Chicago, Illinois, March 16–19, 2003, The Combustion Institute, Pittsburgh, 2003.

[19] J.-Y. Ren, F.N. Egolfopoulos, T.T. Tsotsis, Combust. Sci. Technol. 174 (2002) 181–205.

[20] P. Clavin, G. Joulin, Combust. Theory Modelling 1 (1997) 429–446.

[21] F.N. Egolfopoulos, Proc. Combust. Inst. 25 (1994) 1365–1373.

[22] J.H. Chen, H.G. Im, Proc. Combust. Inst. 27 (1998) 819–826.

[23] C.J. Sung, C.K. Law, Combust. Flame 123 (2000) 375–388.

[24] A. Trouvé, T. Poinsot, J. Fluid Mech. 278 (1994) 1–31.

[25] N. Peters, J. Fluid Mech. 384 (1999) 107–132.

[26] J.Ø. Hinze, Turbulence, McGraw–Hill, New York, 1975.

[27] R.S. Cant, C.J. Rutland, A. Trouvé, in: Proc. Summer Program 1990, Center for Turbulence Research, Stanford, 1990, pp. 271–279.

[28] C.A. Kennedy, M.H. Carpenter, Appl. Numer. Math. 14 (1994) 397–433.

[29] C.A. Kennedy, M.H. Carpenter, R.M. Lewis, Appl. Numer. Math. 35 (2000) 315–357.

[30] T. Poinsot, S.J. Lele, Comput. Phys. 101 (1992) 104–129.

[31] M.D. Smooke, V. Giovangigli, Lect. Notes Phys. 384 (1991) 1–28.

[32] G.P. Smith, D.M. Golden, M. Frenklach, N.W. Moriarty, B. Eiteneer, M. Goldenberg, C.T. Bowman, R.K. Hanson, S. Song, W.C. Gardiner Jr., V.V. Lissianski, Z. Qin, available at: http://www.me.berkeley.edu/gri_mech/.

[33] Y. Ju, H. Guo, K. Maruta, F. Liu, J. Fluid Mech. 342 (1997) 315–334.

[34] R.J. Kee, J.F. Grcar, M.D. Smooke, J.A. Miller, A Fortran Program for Modeling Steady Laminar One-Dimensional Premixed Flames, Tech. Rep. SAND85-8240, Sandia National Laboratories, 1985.

[35] A.E. Lutz, R. Kee, J.F. Grcar, F.M. Rupley, OPPDIF: A Fortran Program for Computing Opposed-Flow Diffusion Flames, Tech. Rep. SAND96-8243, Sandia National Laboratories, 1997.

[36] R.J. Kee, F.M. Rupley, E. Meeks, J.A. Miller, Chemkin III: A Fortran Chemical Kinetics Package for the Analysis of Gas-Phase Chemical and Plasma Kinetics, Tech. Rep. SAND96-8216, Sandia National Laboratories, 1996.

[37] R.J. Kee, G. Dixon-Lewis, J. Warnatz, M.E. Coltrin, J.A. Miller, A Fortran Computer Code Package for the Evaluation of Gas-Phase Multicomponent Transport Properties, Tech. Rep. SAND86-8246, Sandia National Laboratories, 1986.

[38] C.J. Sung, C.K. Law, J.-Y. Chen, Combust. Flame 25 (2001) 906–919.

[39] Y. Ju, T. Niioka, Combust. Flame 99 (1994) 240–246.

[40] C. Safta, C.K. Madnia, in: Proceedings of the 3rd Joint Meeting of the U.S. Sections of the Combustion Institute, Chicago, IL, March 16–19, 2003, The Combustion Institute, Pittsburgh, 2003.

[41] C.J. Sung, C.K. Law, J.-Y. Chen, Proc. Combust. Inst. 27 (1998) 295–304.

[42] T. Echekki, J.H. Chen, Combust. Flame 106 (1996) 184–202.

[43] S.S. Girimaji, S.B. Pope, J. Fluid Mech. 234 (1992) 247–277.

[44] D.C. Haworth, T.J. Poinsot, J. Fluid Mech. 244 (1992) 405–436.

[45] M. Baum, T.J. Poinsot, D.C. Haworth, N. Darabiha, J. Fluid Mech. 281 (1994) 1–32.

[46] H.G. Im, J.H. Chen, Combust. Flame 131 (2002) 246–258.

[47] J.H. Chen, H.G. Im, Proc. Combust. Inst. 28 (2000) 211–218.

[48] S.H. Sohrab, Z.Y. Ye, C.K. Law, Proc. Combust. Inst. 20 (1984) 1957–1965.